Physica C 469 (2009) 491–497

Contents lists available at ScienceDirect

Physica C

journal homepage: www.elsevier.com/locate/physc

Electronic properties of iron arsenic high temperature superconductors revealed by angle resolved photoemission spectroscopy (ARPES)

Chang Liu [a], Takeshi Kondo [a], A.D. Palczewski [a], G.D. Samolyuk [a], Y. Lee [a], M.E. Tillman [a], Ni Ni [a], E.D. Mun [a], R. Gordon [a], A.F. Santander-Syro [b,c], S.L. Bud'ko [a], J.L. McChesney [d], E. Rotenberg [d], A.V. Fedorov [d], T. Valla [e], O. Copie [f], M.A. Tanatar [a], C. Martin [a], B.N. Harmon [a], P.C. Canfield [a], R. Prozorov [a], J. Schmalian [a], A. Kaminski [a,*]

[a] Ames Laboratory and Department of Physics and Astronomy, Iowa State University, Ames, IA 50011, USA
[b] Laboratoire Photons Et Matière, UPR-5 CNRS, ESPCI, 10 rue Vauquelin, 75231 Paris Cedex 5, France
[c] Labratoire de Physique des Solides, UMR-8502 CNRS, Universitè Paris-Sud, Baàt. 510, 91405 Orsay, France
[d] Advanced Light Source, Berkeley National Laboratory, Berkeley, CA 94720, USA
[e] Condensed Matter Physics and Materials Science Department, Brookhaven National Laboratory, Upton, NY 11973, USA
[f] Unitè Mixte de Physique CNRS/Thales, Route dèpartementale 128, 91767 Palaiseau Cedex, France

ARTICLE INFO

Article history:
Available online 20 March 2009

PACS:
74.70.−b
74.25.Jb
79.60.−i

ABSTRACT

We present an overview of the electronic properties of iron arsenic high temperature superconductors with emphasis on low energy band dispersion, Fermi surface and superconducting gap. ARPES data is compared with full-potential linearized plane wave (FLAPW) calculations. We focus on single layer $NdFeAsO_{0.9}F_{0.1}$ (R1111) and two layer $Ba_{1-x}K_xFe_2As_2$ (B122) compounds. We find general similarities between experimental data and calculations in terms of character of Fermi surface pockets, and overall band dispersion. We also find a number of differences in details of the shape and size of the Fermi surfaces as well as the exact energy location of the bands, which indicate that magnetic interaction and ordering significantly affects the electronic properties of these materials. The Fermi surface consists of several hole pockets centered at Γ and electron pockets located in zone corners. The size and shape of the Fermi surface changes significantly with doping. Emergence of a coherent peak below the critical temperature T_c and diminished spectral weight at the chemical potential above T_c closely resembles the spectral characteristics of the cuprates, however the nodeless superconducting gap clearly excludes the possibility of *d*-wave order parameter. Instead it points to *s*-wave or extended *s*-wave symmetry of the order parameter.

1. Introduction

The discovery of superconductivity in oxypnictides [1–3] and later in oxygen free iron arsenic compounds [4,5] created a new, very vibrant field of research. Rather high critical superconducting transition temperatures (~50 K) and upper critical fields (~100 T) combined with highly ductile mechanical properties make these materials very promising for practical applications. From a scientific perspective these materials are providing us with an absolutely fascinating new playground for studying the relation between magnetism and superconductivity. This prompted significant experimental [6–32] and theoretical [33–44] effort to understand the physics governing their interesting properties and the (most likely exotic) mechanism of superconductivity. The undoped, non-superconducting systems of both oxygen containing RFeAsO (R = La, Nd, Sm) and oxygen free BFe_2As_2 (B = Ba, Sr, Ca) display structural [1,8,5,9,10] and magnetic [6,7] phase transitions at elevated temperatures. Doping RFeAsO with fluorine (electron doping) as well as BFe_2As_2 with potassium (hole doping) or substitution the Fe with either Nickel (electron doped) or Cobalt (hole doped) leads to a suppression of the structural and magnetic transition temperature. This extends the tetragonal phase down to low temperatures and leads to the emergence of superconductivity [1–5]. Understanding the electronic properties of both high and low temperature phases and symmetry of the order parameter is therefore instrumental to uncover the mechanism of the superconductivity in these materials.

2. Experimental details – crystal growth

Single crystals of the parent compound, $BaFe_2As_2$, and potassium-doped samples, $Ba_{1-x}K_xFe_2As_2$, with an approximate doping $x = 0.45$ were grown out of a Sn flux using conventional high temperature solution growth techniques [5]. Large (up to 2 ×2 mm) single crystals were cleaved *in situ* yielding flat mirror-like sur-

* Corresponding author.
E-mail address: kaminski@ameslab.gov (A. Kaminski).

0921-4534/$ - see front matter © 2009 Elsevier B.V. All rights reserved.
doi:10.1016/j.physc.2009.03.050

faces. High pressure synthesis of $NdFeAsO_{0.9}F_{0.1}$ samples was carried out in a cubic, multi-anvil press, with an edge length of 19 mm from Rockland Research Corporation. Stoichiometric amounts of $NdFe_3As_3$, Nd_2O_3, NdF_3 and Nd were pressed into a pellet with a mass of approximately 0.5 g and placed inside of a BN crucible with an inner diameter of 5.5 mm. The synthesis was carried out at a pressure of 3.3 GPa. The temperature was increased, over 1 h, from room temperature to 1350–1400 °C and then held there for 8 h before being quenched to room temperature. The pressure was then released and the sample was removed mechanically. This synthesis produced a high density pellet that contained large grains (up to 300 × 200 μm in cross-section [27]) of superconducting ($T_c \sim 53$ K) $NdFeAsO_{0.9}F_{0.1}$ as well as non-superconducting NdOFeAs. In addition there are inclusions of FeAs and Nd_2O_3. Magneto optical measurements [27] indicate that on average the samples are over 50% superconducting. The single crystals were extracted mechanically from the pellet.

3. Experimental details – ARPES and band calculations

Samples were mounted on Al pins using either Torr seal vacuum epoxy or Epotek HD21D silver epoxy. They were cleaved *in situ* yielding a flat mirror-like surface. ARPES experiments performed at Synchrotron Radiation Center (SRC) utilized Scienta SES2002 end station on the PGM beam line with photon energies 20–77 eV, ~100 μm beam and energy resolution set at 16 meV. Experiments at Ames Laboratory were performed using ultra-high resolution ARPES spectrometer consisting of a Scienta SES2002 analyzer, GammaData ECR UV source and custom designed refocusing optics with 1 mm beam, 21.2 eV (He I) and 40.8 eV (He II) photons with the energy resolution set to 5 meV. Experiments at Advanced Light Source were performed using beamlines 7.0.1 (SES4000) with 50 μm beam size and resolution set at 30 meV. Fermi energy was determined using the spectral edge of evaporated Au or Al in electrical contact with the sample. Our full-potential linearized plane wave (FLAPW) calculations [44] used the local density approximation (LDA) [45], and the experimental lattice constants [4] for the undoped parent compound $BaFe_2As_2$ and potassium-doped $Ba_{1-x}K_xFe_2As_2$ with $x = 0.4$. Total energy minimization was used to determine the z location of the arsenic atom $z_{As} = 0.341c$.

4. Electronic properties of $NdFeAsO_{0.9}F_{0.1}$

There is significantly less data available on the electronic structure of R111 [21,20] systems mainly due to the lack of availability of large single crystals that are essential for an accurate determination of the electronic structure. The presence of multiple phases in polycrystalline samples can often contaminate the pristine spectra. As an example we plot in Fig. 1a a comparison of the photoemission data from polycrystalline samples and angle integrated measurements from single crystals. The strong intrinsic peak just below the chemical potential is very strongly suppressed in the polycrystalline samples. A common method for illustrating the topology of the Fermi surface is to plot the ARPES intensity at the chemical potential as a function of momentum [46,47]. In Fig. 1b and d we plot the ARPES intensity integrated within 20 meV about the chemical potential from data obtained using 22 eV and 77 eV photons. The brightest areas in these plots indicate high photoelectron intensity and therefore approximate to the location of the Fermi surface. To obtain more accurate information we have extracted the exact locations of the Fermi momentum from momentum distribution curves (MDCs) using a procedure described elsewhere [47] and plot them in panels 1 (c) and (e). Our data show that indeed this system has a Fermi surface that consists of two main contours: a larger one centered at $\Gamma(0,0)$ and a smaller one centered at the corners of the Brillouin zone. For comparison we plot the 3-dimensional (3D) Fermi surfaces based on FLAPW band calculations for $NdFeAsO_{1-x}F_x$ with $x = 0.1$ in Fig. 1f. A 2D cut at Γ ($k_z = 0$) is shown in Fig. 1g. We note that there are both similarities and differences between the data and calculations. Overall the calculation predicts Fermi surface sheets centered at Γ and M, in agreement with our measurements. The main difference between theory and experiment is the number and relative

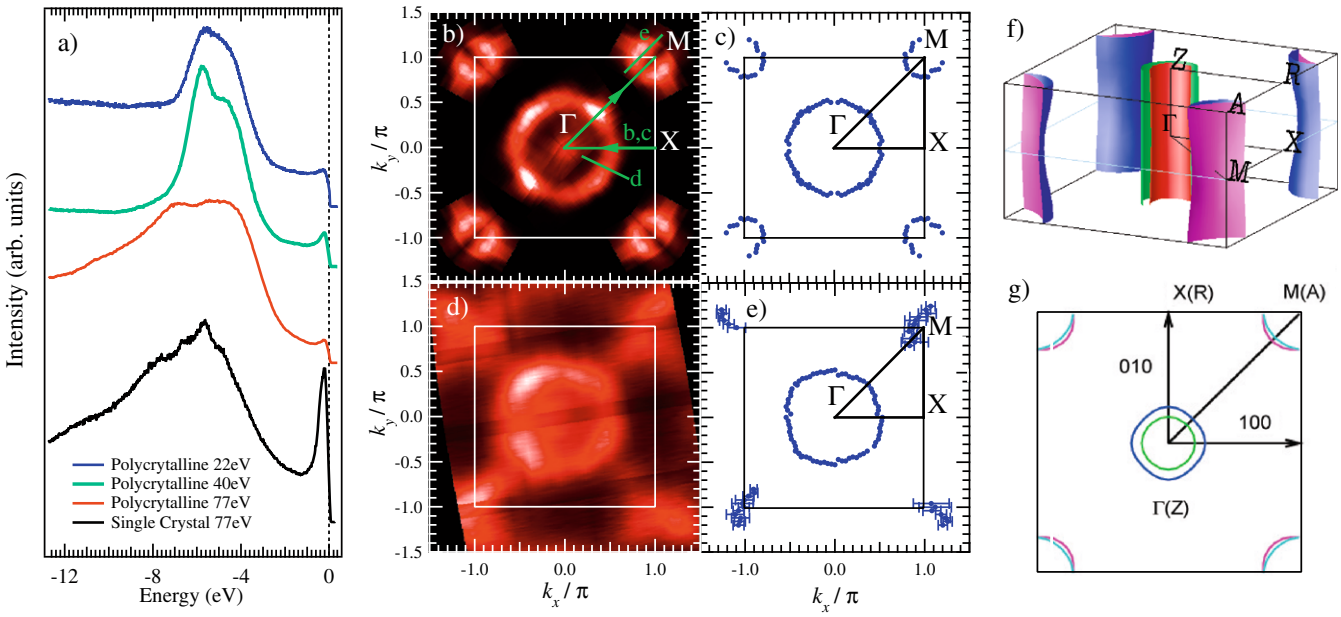

Fig. 1. Measured and calculated Fermi surface of $NdFeAsO_{1-x}F_x$. (a) Angle intergrated spectra from polycrystalline and single crystal samples for selected photon energies. (b) Fermi surface map – intensity of the photoelectrons integrated over 20 meV about the chemical potential obtained with 22 eV photons at $T = 70$ K. The areas of bright color mark the locations of the Fermi surface. (c) The locations of the Fermi crossings extracted from the raw data by fits to the MDCs. (d) same data as in (b) but obtained with 77 eV photons. (e) Same data as in (c) but obtained with 77 eV photons. (f) 3-Dimensional FS of $NdFeAsO_{1-x}F_x$ with $x = 0.1$ obtained from FLAPW calculations. (g) A FS cross-section at $k_z = 0$ (X–Γ–M plane) obtained by FLAPW calculations.

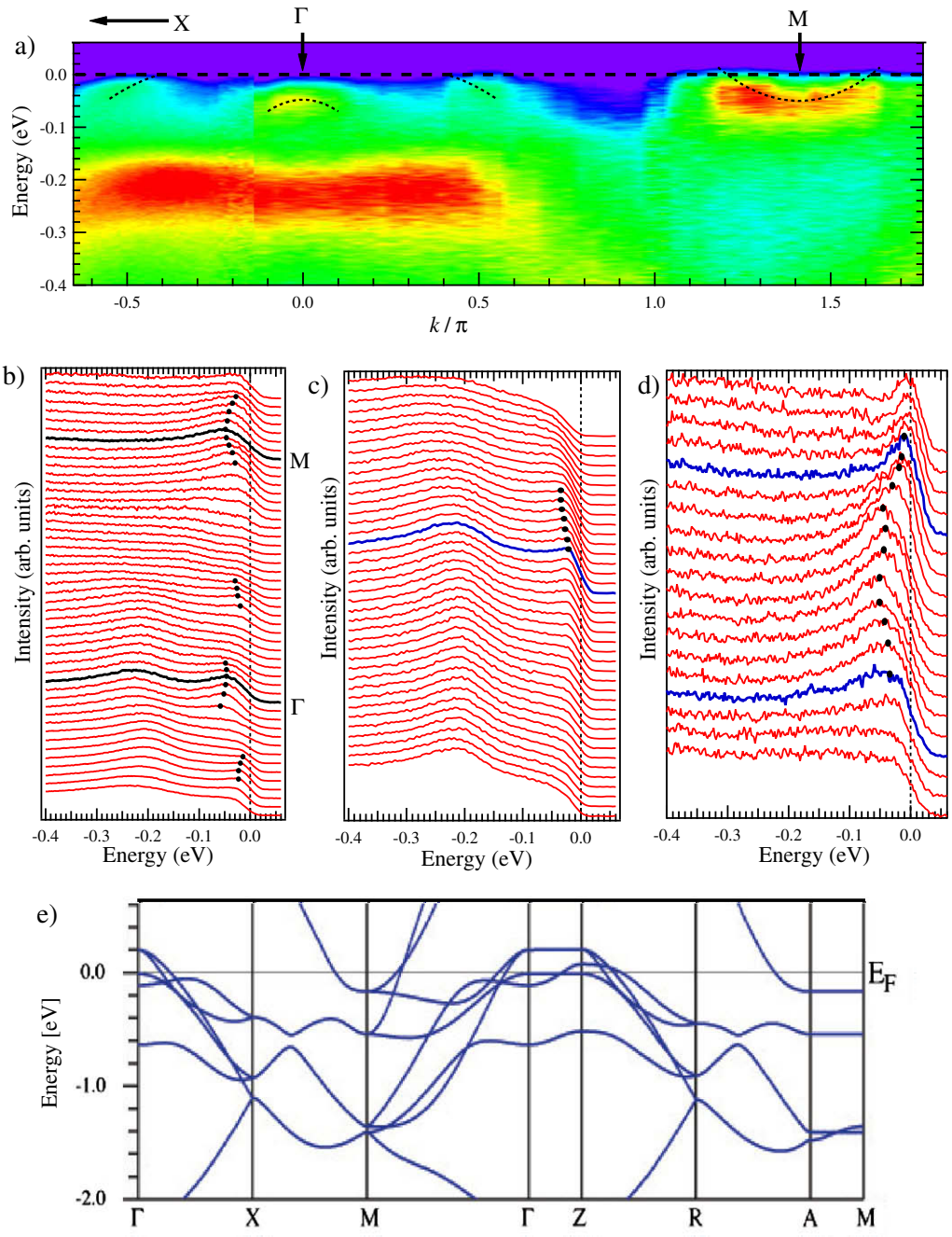

Fig. 2. Measured and calculated band dispersion of $NdFeAsO_{0.9}F_{0.1}$. Locations of the cuts are indicated by green lines in Fig. 1b. (a) Measured ARPES intensity along the X–Γ–M direction (T = 70 K). Black dashed curves are guides to the eye. (b) Energy distribution curves (EDCs) for data in panel a) at T = 70 K. (c) and (d) EDCs (T = 70 K) in the directions shown in Fig. 1b. Blue curves mark the Fermi crossing momenta k_F. (e) Band dispersion along the symmetry directions for $NdFeAsO_{1-x}F_x$ with x = 0.1 obtained from FLAPW calculations.

size of the FS sheets. According to calculation there should be two sheets around each symmetry point. It is quite possible that the separation between the sheets is smaller than the calculated result and not sufficient to resolve in the experiment. A second disagreement is in the size of the Γ-pocket. Experimentally the FS "tube" crosses the band(s) about half-way from Γ to X, while theory has the band crossing E_F at about 0.27 of the Γ to X distance [Fig. 1g]. This qualitative disagreement between theory and experiment can have a number of origins. The band calculation are very sensitive to the distance between the Fe–As ionic sites. On the other hand surface sensitivity of ARPES can also play a role.

The band dispersion along selected cuts (indicated by [1]green arrows in Fig. 1b is shown in Fig. 2. Panel 2 (a) shows the intensity map along the X–Γ–M symmetry line. Bright areas on this graph mark the locations of the bands. From these data we can identify the topology of the main Fermi surface components. The Fermi surface centered at Γ is hole-like, i.e., the unoccupied states are on the top of this band. In contrast, the Fermi surface centered at M is electron-like with the

[1] For interpretation of color in Figs. 2, 3 and 5, the reader is referred to the web version of this article.

bottom of the band located at ~50 meV below the chemical potential. In addition to these two conduction bands, there are also two very prominent fully occupied bands at this particular incident photon energy. The tops of both are centered at Γ. The first is located just 50 meV below the chemical potential. The second band has a rather flat top which is located at ~200 meV below the chemical potential. This band is most likely responsible for the strong peak in angle integrated measurements. Energy distribution curves (EDCs) for the above data are shown in panel (b). The dispersion of the peaks in this plot agrees with the above description of the Fermi surface topology. The band dispersion close to the chemical potential for the Γ-pocket and M pocket are plotted in panels 2 (c and d), respectively. The location of the Fermi momenta are marked by blue solid lines. In panel 2 (e) the calculated band structure along high symmetry directions for $NdFeAsO_{1-x}F_x$ ($x = 0.1$) is presented for comparison.

We now proceed to discuss the symmetry of the superconducting gap along the Γ-pocket. A plot of the ARPES intensity integrated over ± 20 meV about the Fermi energy as a function of momentum [46,47] is shown in Fig. 3a. We focus on two different Fermi momentum points along the high symmetry directions, Γ–X and Γ–M, respectively (marked with blue and red dots, respectively). The ARPES intensity along Γ–M cut is shown in Fig. 3b as a function of momentum and energy for $T = 20$ K, deep in the superconducting state. At first glance this plots exhibit all the char-

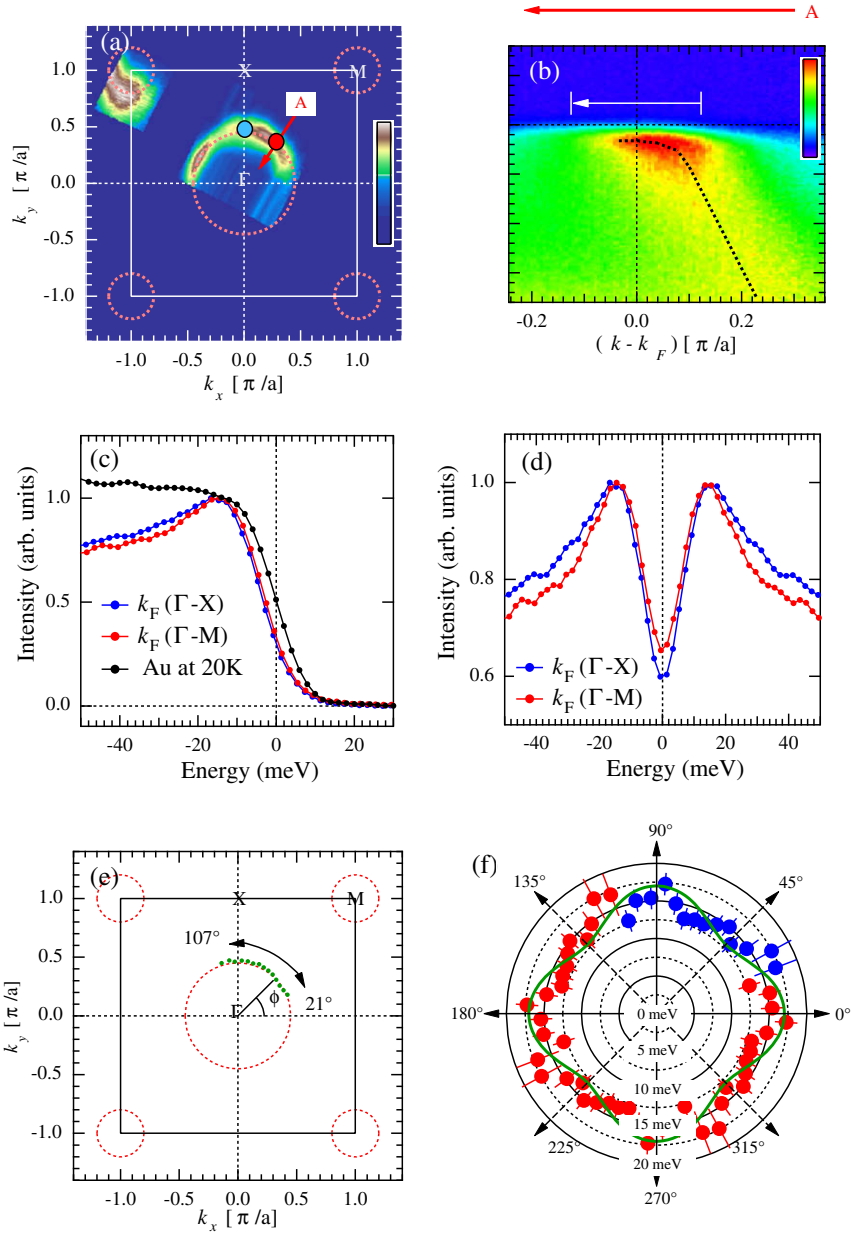

Fig. 3. The magnitude of the superconducting gap along the Γ hole pocket of $NdFeAsO_{0.9}F_{0.1}$. Panels adopted from Ref. [20]. (a) ARPES intensity at the chemical potential. Bright areas mark location of the Fermi surface. (b) ARPES intensity ($T = 20$ K) along a Γ–M cut indicated with red arrow in (a). Dotted line is a guide to an eye that marks band dispersion. (c) Comparison of the EDC's in superconducting state along Γ–X and Γ–M directions. (d) Symmetrized EDCs from the data in panel (c). (e) Schematic diagram of the Brilloiun zone with green dots marking points where superconducting gap was measured and definition of Fermi surface angle ϕ. (f) Magnitude of the superconducting gap around the Γ-pocket in polar coordinates. It is clear from this graph that the gap is always open, with a magnitude (Δ_{peak}) that varies between ~13 meV and ~18 meV, indicating conventional s-wave or slightly anisotropic s-wave behavior at the Γ-pocket. The green line indicates a model with a slight gap anisotropy of 20% that would still be consistent with this data.

acteristics of a sample in the superconducting state: a buildup of intensity just below the chemical potential in shape of an arc due to formation of superconducting coherent peak and particle-hole mixing [48]. This peak appears only below T_c in fashion similar to one reported in cuprates [49,50]. The width of the coherent peak (~20 meV) is mostly limited by the experimental energy resolution. In order to compare the gap sizes along the two different directions, we plot the EDCs in Fig. 3c and the corresponding symmetrized EDCs in Fig. 3d. The superconducting gap can be easily estimated from the EDC data by either fitting a BCS-like spectral function [51] or evaluating the binding energy of the coherent peak. It should be noted that both methods yield very similar results. We found that the superconducting gap has a comparable value $\sim 15 \pm 1.5$ meV in both directions. The gap along Γ–X appears slightly bigger than along the Γ–M direction (all data points of the peak are further from the chemical potential and the dip is larger), however we cannot conclude this with great certainty given the experimental error bars. We measured the ARPES spectra at a multiple Fermi momenta points around the Γ-centered hole pocket (Γ-pocket), in order to obtain the symmetry of the superconducting gap. We covered a wide range of the Fermi surface angle ($21° \leqslant \phi \leqslant 107°$), which is roughly a quarter of the Fermi surface as shown in Fig. 3e. The results are shown in Fig. 3f in polar coordinates. To give a better sense of the gap symmetry we copied the results from one quadrant into the other three quadrants using the crystal symmetry axes. We use blue symbols to mark the measured data and red ones to indicate the data points that are a reflection of the actual data. The superconducting gap is never zero around the Fermi surface, indicating a lack of nodes. This excludes simple *p*- or *d*-wave pairing scenarios, which have nodes on the Fermi surface. In the simplest scenario, our data is consistent with isotropic *s*-wave behavior, however we cannot exclude the possibility of a small anisotropy being present of order of 20% due to the finite error bars.This would also be consistent with a pairing state with nodes of the gap-function between distinct sheets of the Fermi surface. Such an anisotropic gap is indicated in Fig. 3f by the green line which shows a 20% anisotropy and lies within the error bars of our experiment in agreement with penetration depth measurements [28,29]. To distinguish between the subtle signatures of this limited subset of models, an additional ARPES study with significantly smaller error bars is necessary. However, our data already clearly excludes pairing states with gap nodes on the Fermi surface.

5. Electronic properties of $Ba_{1-x}K_xFe_2As_2$ (B122) with $x = 0$ and $x = 0.45$

The recent growth of large, high quality single crystals of $BaFe_2As_2$ (B122, where B = Ba, Sr or Ca) [5] has opened up the possibility of examining the electronic properties of these materials more readily than the R111 system. Here we focus on the electronic structure of undoped and potassium-doped $BaFe_2As_2$. In Fig. 4a and b we plot the integrated ARPES intensity within 20 meV energy range about the chemical potential for undoped and K-doped samples. The Fermi surface of undoped $BaFe_2As_2$ consists of a smaller hole pocket centered at Γ and larger electron pockets at X points, whose spectrum at two corners in the $k_{1,-1,0}$ direction is somewhat more intense. In the potassium-doped samples (Fig. 4b) the Γ-pocket becomes larger and the X-pocket shrinks, which is consistent with hole doping of carriers. In Fig. 4c we plot the Fermi surface map obtained with 100 eV photons over several Brillouin zones. We note that the X-pockets in doped samples have a characteristic "starrish" shape, resembling to a degree results of FLAPW calculations. The variation of intensity around each contour of both Γ- and X-pockets is most likely due to photoemission matrix elements.

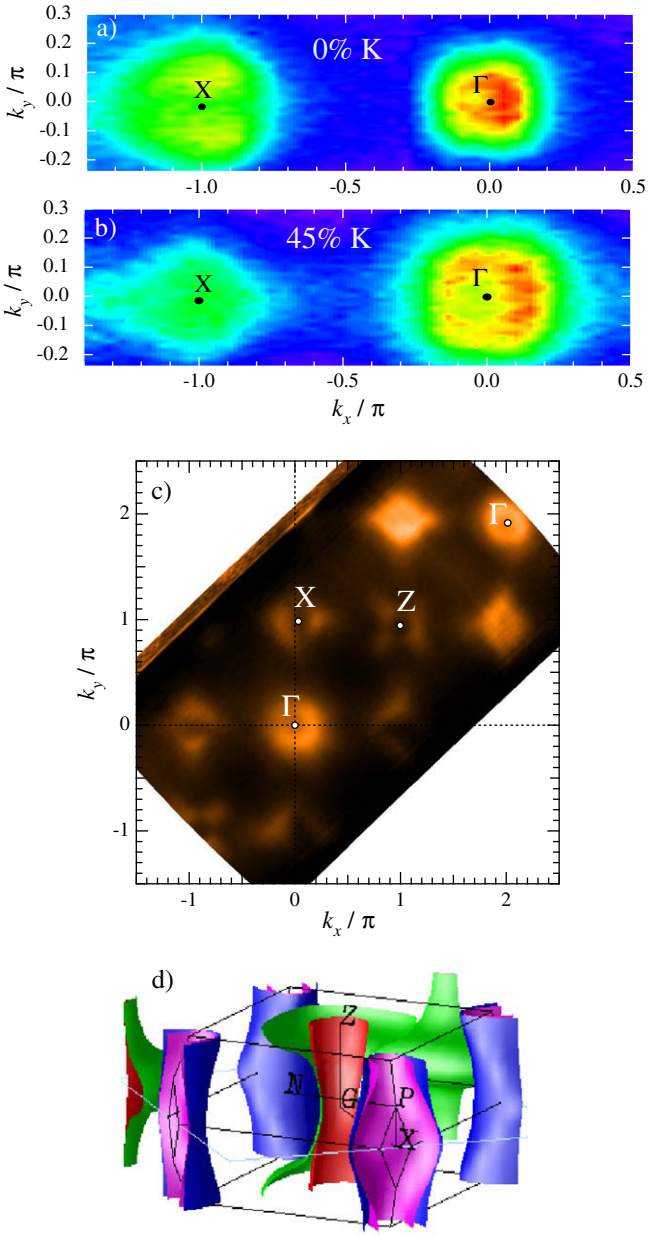

Fig. 4. Measured Fermi surface (FS) of $BaFe_2As_2$ and $Ba_{1-x}K_xFe_2As_2$ and calculated FS for undoped case. Panels (a) and (b) adopted from Ref. [21]. (a) FS map of $BaFe_2As_2$ – intensity of the photoelectrons integrated over 20 meV about the chemical potential obtained with 40.8 eV photons. Experiment was done at $T = 100$ K. Areas of bright color mark the locations of the FS. (b) FS map of $Ba_{1-x}K_xFe_2As_2$ with nominal $x = 0.45$ measured under the same conditions as (b). (c) FS map of $BaFe_2As_2$ obtained with 100 eV photons over several Brillouin zones. (d) 3-Dimensional FS of $Ba_{1-x}K_xFe_2As_2$ for $x = 45\%$ at $T = 40$ K obtained from FLAPW calculations.

In Fig. 5 we plot the experimental band dispersion data perpendicular to the Γ–X direction along cuts through the X and Γ points (i.e. along the $k_{1,-1,0}$ direction). For both the $x = 0$ and $x = 0.45$ doping levels, the hole pockets at Γ and the electron pockets at X are shown and are in general agreement with band calculations. Here, we can examine the relative size of the hole pockets and the electron pockets in more detail by studying the Fermi crossing momenta (k_Fs) marked by blue curves in Fig. 5c, d, h and i. These k_Fs were determined from the most intense points in the MDCs at the Fermi level. The number of EDCs between two k_Fs is proportional to the actual size of each pocket. The calculated Fermi sur-

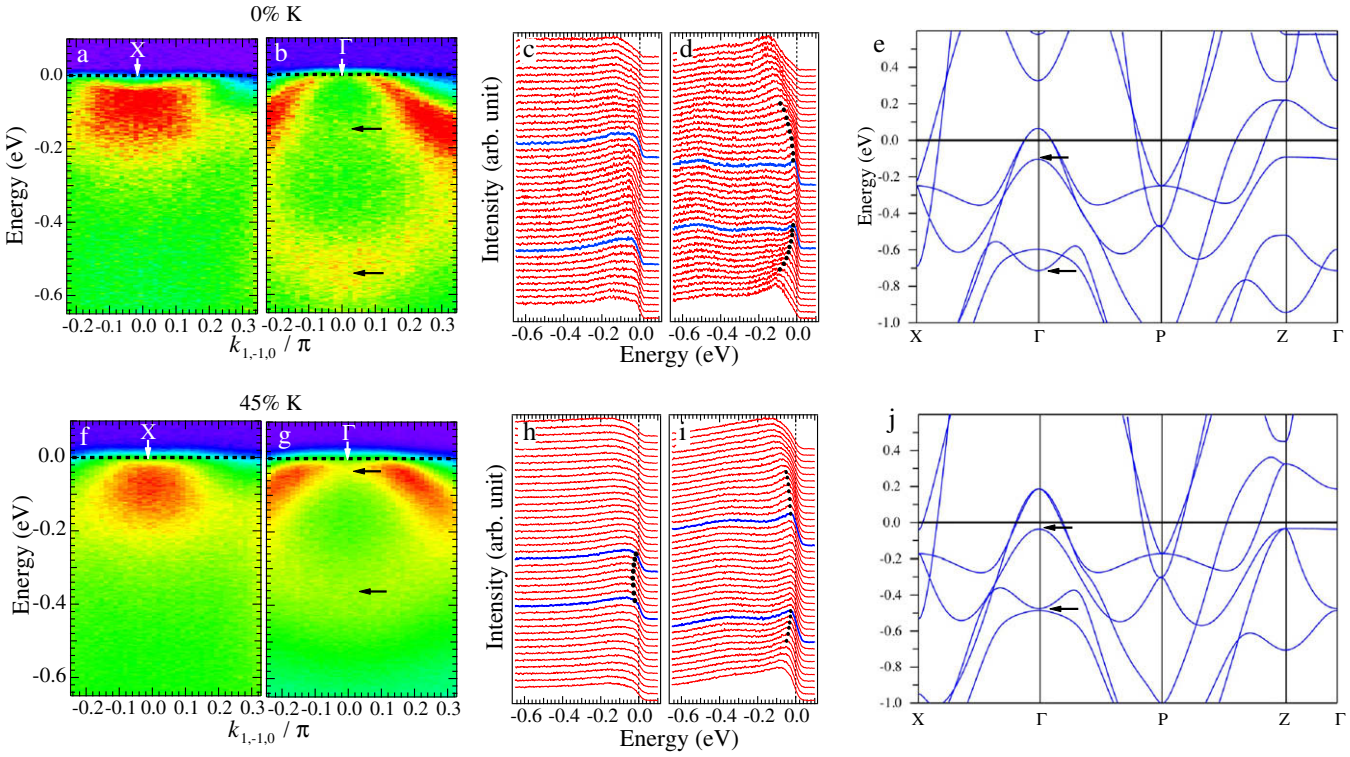

Fig. 5. Experimental band dispersions and corresponding energy distribution curves (EDCs) along selected cuts, compared with theoretical band structure. Panels (a)–(d) present the data of undoped $BaFe_2As_2$, while panels (e)–(h) present the data of $Ba_{1-x}K_xFe_2As_2$ with nominal $x = 0.45$. Panels adopted from Ref. [21]. (a) ARPES intensity map in X region for undoped sample. (b) ARPES intensity map in Γ region for undoped sample. (c) and (d) EDC's for same cuts as in (a) and (b). Curves at Fermi momentum are marked blue. (e) Results of FLAPW band calculation for parent compound $BaFe_2As_2$. (f) ARPES intensity map in X region for doped sample $x = 0.45$. (g) ARPES intensity map in Γ region for doped sample $x = 0.45$. (h) and (i) EDC's for same cuts as in (f) and (g). Curves at Fermi momentum are marked blue. (e) Results of FLAPW band calculation for doped $Ba_{1-x}K_xFe_2As_2$ with $x = 0.45$.

face of $BaFe_2As_2$ (Fig. 5e) resembles one for LaFeAsO [33,34]. The band structure for undoped $BaFe_2As_2$ is shown in Fig. 5e and one calculated for doped case using virtual crystal method is shown in Fig. 5j. Clearly, in the undoped parent compound both in experimental data as well as calculation the X-pocket is larger than the Γ-pocket, whereas in the $x = 0.45$ potassium-doped samples, the opposite is the case. This effect is consistent with the idea of rigid-band shifting, namely, potassium doping lowers the chemical potential of the parent compound, while the shapes of the bands are left unchanged. A second notable doping dependent feature is the energy shift of two fully occupied bands, marked by black arrows in Fig. 5b, e, g and j, where Fig. 5 e and j plot the calculated band structure of undoped $BaFe_2As_2$ and potassium-doped $Ba_{1-x}K_xFe_2As_2$ with $x = 0.45$, respectively. These arrows point to similar characteristic features in experimental data and calculations and how they change upon doping. On potassium doping, the upper band shifts to lower binding energy by ~130 meV, while the lower band shifts to lower binding energy by ~180 meV. This fact is in qualitative agreement with band structure calculations. A third feature notable in Fig. 5 is the missing of bilayer splitting in the measured data. Most likely this is due to extrinsic broadening of the ARPES lineshape. All these doping dependent features point to the conclusion that the FLAPW approximation is valid in both undoped and hole-doped iron arsenic superconductors.

6. Conclusions and outlook

We examined the electronic structure and properties of the R111 and B122 iron arsenic superconductors. We find fair resemblance between measured and calculated band structure and Fermi surface. At present it is difficult to establish the degree of the similarity. While several different interpretations of very broad features in terms of band dispersion and Fermi surface have been proposed [18,19,22,23,25], it is not possible at present to distinguish between these scenarios. This applies in particular to the shape of the electron pocket surrounding the $X(M)$ points as well as the number of bands forming hole pockets around the Γ point. The origin of significant broadening is not known, but most likely it is extrinsic and related to either condition of the cleaved surface or crystal quality. Certainly more experimental effort is required to establish the shape of the electron pocket Fermi surface and the exact band dispersion in these materials.

In R111 system we find nodeless superconducting gap consistent with results of recent penetration depth measurements [28,29]. In R122 system the situation is more complicated, as ARPES reports nodeless superconducting gap, while penetration depth measurements support existence of nodes [30,32]. A possible explanation is that the superconducting gap does not have nodes at the particular k_z location studied by ARPES [19,24], however nodes do exist at other points along the k_z axis. Further detailed studies involving larger range of momenta is required to resolve this disagreement.

Acknowledgements

Work at Ames Laboratory was supported by the Department of Energy – Basic Energy Sciences under Contract No. DE-AC02-07CH11358. The Synchrotron Radiation Center is supported by the NSF contract DMR-0537588. ALS is operated by the US DOE under Contract No. DE-AC03-76SF00098. Brookhaven National Laboratory is supported by US DOE under Contract No. DE-AC02-98CH10886. A.F.S.S. thanks LPEM for financial support.

References

[1] Y. Kamihara et al., J. Am. Chem. Soc. 130 (2008) 3296.
[2] H. Takahashi et al., Nature 453 (2008) 376.
[3] Z.A. Ren et al., Chin. Phys. Lett. 25 (2008) 2215.
[4] M. Rotter et al., Phys. Rev. Lett. 101 (2008) 107006.
[5] N. Ni et al., Phys. Rev. B 78 (2008) 014507.
[6] J. Dong et al., Europhys. Lett. 83 (2008) 27006.
[7] Clarina de la Cruz et al., Nature 453 (2008) 899.
[8] M. Rotter et al., Phys. Rev. B 78 (R) (2008) 020503.
[9] J.-Q. Yan et al., Phys. Rev. B 78 (2008) 024516.
[10] N. Ni et al., Phys. Rev. B 78 (2008) 014523.
[11] Y. Qiu et al., Phys. Rev. Lett. 101 (2008) 257002.
[12] A.I. Goldman et al., Phys. Rev. B 78 (2008) 100506.
[13] A. Kreyssig et al., Phys. Rev. B 78 (2008) 184517.
[14] A.D. Christianson et al., Phys. Rev. Lett. 101 (2008) 157004.
[15] R.J. McQueeney et al., Phys. Rev. Lett. 101 (2008) 227205.
[16] T.Y. Chen et al., Nature 453 (2008) 1224.
[17] C. Liu et al., 2008, arXiv:0806.2147.
[18] L.X. Yang et al., Phys. Rev. Lett. 102 (2009) 107002.
[19] H. Ding et al., Europhys. Lett. 83 (2008) 47001.
[20] Takeshi Kondo et al., Phys. Rev. Lett. 101 (2008) 147003.
[21] Chang Liu et al., Phys. Rev. Lett. 101 (2008) 177005.
[22] V.B. Zabolotnyy et al., Nature 457 (2009) 569.
[23] D.V. Evtushinsky et al., 2008, arXiv:0809.44552008.
[24] L. Wray et al., Phys. Rev. B 78 (2008) 184508.
[25] D. Hsieh et al., 2008, arXiv:0812.2289.
[26] A.I. Coldea et al., Phys. Rev. Lett. 101 (2008) 216402.
[27] R. Prozorov et al., New J. Phys. 11 (2009) 035004.
[28] L. Malone et al., 2008, arXiv:0806.3908.
[29] C. Martin et al., 2009, arXiv:0903.2220.
[30] R.T. Gordon et al., Phys. Rev. Lett. 102 (2009) 127004.
[31] J.D. Fletcher et al., 2008, arXiv:0812.3858.
[32] R.T. Gordon et al., Phys. Rev. B 79 (2009) 100506(R).
[33] D.J. Singh, M.-H. Du, Phys. Rev. Lett. 100 (2008) 237003.
[34] I.A. Nekrasov et al., JETP Lett. 88 (2008) 144.
[35] V. Cvetkovic et al., Europhys. Lett. 85 (2009) 37002.
[36] I.I. Mazin et al., Phys. Rev. Lett. 101 (2008) 057003.
[37] G. Xu et al., Europhys. Lett. 82 (2008) 67002.
[38] D.J. Singh et al., Phys. Rev. Lett. 100 (2008) 237003.
[39] Z.Y. Weng, 2008, arXiv:0804.3228.
[40] F. Wang et al., 2008, arXiv:0805.3343.
[41] Y. Ran et al., Phys. Rev. B 79 (2009) 014505.
[42] Y. Ran et al., 2008, arXiv:0806.2321.
[43] F. Wang et al., Phys. Rev. Lett. 102 (2009) 047005.
[44] P. Blaha et al., An augmented plane wave + local orbitals program for calculation crystal properties. (K. Schwarz, TU Wien, Austria, 2001) ISBN: 3-9501031-1-2.
[45] J.P. Perdew, Y. Wang, Phys. Rev. B 45 (1992) 13244;
J.P. Perdew, Y. Wang, J. Alloys Compd. 302 (2000) 70.
[46] H.M. Fretwell et al., Phys. Rev. Lett. 84 (2000) 4449.
[47] J. Mesot et al., Phys. Rev. B 63 (2001) 224516.
[48] J.C. Campuzano et al., Phys. Rev. B 53 (1996) R14737.
[49] A.V. Fedorov et al., Phys. Rev. Lett. 82 (1999) 2179.
[50] D.L. Feng et al., Science 289 (1999) 277.
[51] M.R. Norman et al., Phys. Rev. B 57 (1998) R11093.